Effect of silicon carbide particle (SiCp) addition on the hot deformation behavior of the AZ80 alloy.

Pili Kumari Sahoo, Priya Singh

College of Engineering Bhubaneswar, Biju Pattnaik University of Technology, Odisha, India

Abstract

Using a hot compression test, the effects of a trace (3 vol%) addition of silicon carbide particles (SiCp) on the hot deformation behavior of the magnesium-5% zinc (Mg-5Zn) alloy were investigated. The addition of trace SiCp lowers the activation energy of the Mg-5Zn alloy because the high dislocation density in the particle deformation zone (PDZ) surrounding SiCp promotes pipe diffusion. Furthermore, as the PDZ's size (dPDZ) increases, the composite's activation energy likewise decreases. Furthermore, the processing map indicates that the ideal deformation condition for a 3 vol% 20 mm SiCp/Mg-5Zn composite is 693 K and 0.1 e0.01s~1. As strain increases, the instability region of the processing map at 543 K and 1 s^1 vanishes. This is linked to the trace SiCp's inhibitory effect on {1012} extension twins and its promoting effect on DRX within {1011} contraction twins and {1011}-{1012} double twins by introducing flow localization. Furthermore, using EBSD technology, the DRX behavior of the 3 vol% 20 mm SiCp/Mg-5Zn composite was examined. Particle-stimulated nucleation (PSN), twining dynamic recrystallization (TDRX), and continuous dynamic recrystallization (CDRX) are the composite's DRX mechanisms at 543 K and 1 s^1.

1. Introduction

The mechanical qualities of magnesium (Mg) alloys, such as their high specific strength, excellent damping capabilities, and low density, are advantageous [1,2]. Unfortunately, due to their low modulus, low wear resistance, and poor deformability at room temperature, magnesium alloys have limited applications. The aforementioned drawbacks of magnesium alloys can be addressed by particle reinforced magnesium matrix composites (PMMCs), which may find use in the automotive, defense, and aerospace industries [3].

PMMCs that are as-cast typically have flaws like porosity and shrinkage, which can be fixed with hot deformations. The flow stress has a major impact on PMMCs during the hot deformation process, so it's important to comprehend the hot deformation mechanism. The constitutive equations are typically employed to provide further details on how the flow stress varies with various hot deformation parameters, including strains, temperatures, and strain rates [4]. The stress exponent n and the activation energy Q of deformation can then be calculated to determine the hot deformation mechanism of PMMCs. With n and Q of 5.5 and 176 kJ/mol, respectively, Liu et al.'s [5] analysis of the hot deformation mechanism of the AZ91 alloy revealed that the hot deformation mechanism is the cross-slip of screw

dislocation from basal plane to prismatic plane-controlled dislocation climb. The hot deformation behavior of 10 vol% 10 mm SiCp/AZ91 composites was studied by Wang et al. [6]. The calculated values of n and Q were 5 and 99 kJ/mol, respectively.

The dislocation climb controlled by diffusion at the grain boundary was identified as the hot deformation mechanism. Consequently, more research is required to understand how the composite's hot deformation mechanism relates to the features of the particle distribution. In addition, Prasad's processing map [7] is a potent tool for controlling the microstructure and optimizing the deformation process. According to Li et al. [8], the processing map's peak dissipation efficiency region for a Mg-Li alloy is between 200 and 350 °C and 0.001e1 s-1. Because micro SiCp has more effective dislocation accumulation abilities than nano SiCp, Zhang et al. [9] found that the micro SiCp/AZ91 composite has a wider workability region than the nano SiCp/AZ91 composite.

The 3 vol% 20 mm SiCp/Mg-5Zn composite (lPDZ ¼ ~22 mm and dPDZ ¼ ~60 mm) was made for this investigation. The lPDZ is the same but the dPDZ is larger than the 5 mm 1 vol% SiCp/Mg-5Zn composite (lPDZ ¼ ~24 mm and dPDZ ¼ ~15 mm) in the prior study [20]. Furthermore, the hot compression test was used to examine the true stressestrain curves of the 3 vol% 20 mm composite. Concurrently, the true stress-strain curves serve as the foundation for the construction of the strain-compensated Arrhenius constitutive equation and processing map. EBSD technology was utilized to analyze the microstructure and DRX mechanisms in various regions of the processing map.

2. Experimental Procedure

The Mg-5Zn alloy and SiCp were selected as matrix alloy and reinforcement, respectively. The pure Mg and Zn were supplied by Shanxi Yinguang Huasheng Magnesium Co., Ltd, China. And the SiC p (20 mm, 3 vol%) was purchased from Zhengzhou Baige Technology Co., Ltd., China. Firstly, the Mg-5Zn alloy was prepared by mixing pure Mg and Zn at 1023 K with the protection of CO2 and SF6 mixed gas. Subsequently, the composite was prepared using semisolid stirring assisted ultrasonic vibration. The SiCp was heated to 853 K and poured into the semi-solid Mg-5Zn alloy. After adequately stirring the melt, the temperature was increased to 993 K and insulation for 15 min. Then the ultrasonic process lasted for 15 min under a power of 1 kW to uniformly mix reinforcement particles. Finally, it was poured into a cylindrical steel mold with a diameter of 40 mm and cooled to 673 K to obtain the ingot. Casting defects were not observed in the ingot and the particle distribution is uniform at the macroscopical scale. Besides, the detailed preparation method of this kind of composite has been reported in previous research [21].

Cylindrical compression samples (8 mm diameter and 12 mm height) were machined from the center of the ingot. The uniaxial compression test was conducted on a Gleeble 3800 thermomechanical simulator with a temperature range of 543-693 K and a strain rate range of 0.001-1 s^{-1}. The bottom surface of the samples was lubricated with nickel anti-seize paste to ensure uniform deformation. The Gleeble 3800 thermomechanical simulator was vacuumed

and heated the sample to the design temperature at a speed of 5 K/s, then keeping it for 5 min. The compressed samples were water quenched to retain the deformed microstructure.

The microstructures were observed in the center of deformed samples by scanning electron microscope (SEM, SU8010, HITACHI) and optical microscopy (OM, OLYMPUS GX53). The OM and SEM samples were polished with sandpaper and then chemically etching with 4% oxalic acid (2 g of oxalic acid and 50 mL of distilled water) to show the grain boundaries. Moreover, detailed microstructural characterizations in the center of deformed samples were observed by electron backscattered diffraction (EBSD, JEOL JSM-7000 F operated at 20 kV). The EBSD samples were electro polished with 5% perchloric acid under - 30 °C for 1.5 min. The data of the EBSD was analyzed by the channel 5 software.

3. Results

3.1. True-Stress-Strain Curves

The true stress-strain curves of the SiCp/Mg-5Zn composite deformed to a true strain of 0.69 in the temperature range of 543-693 K and a strain rate range of 10^{-3} s^{-1} are shown in significantly with the increasing temperatures and decreasing strain rates. The thermoplastic deformation process of magnesium alloys is thought of as a thermally activated process [11]. The average kinetic energy and amplitude of the atoms increase with the increasing temperatures, which is conducive to the movement of vacancy migration and dislocation slip.

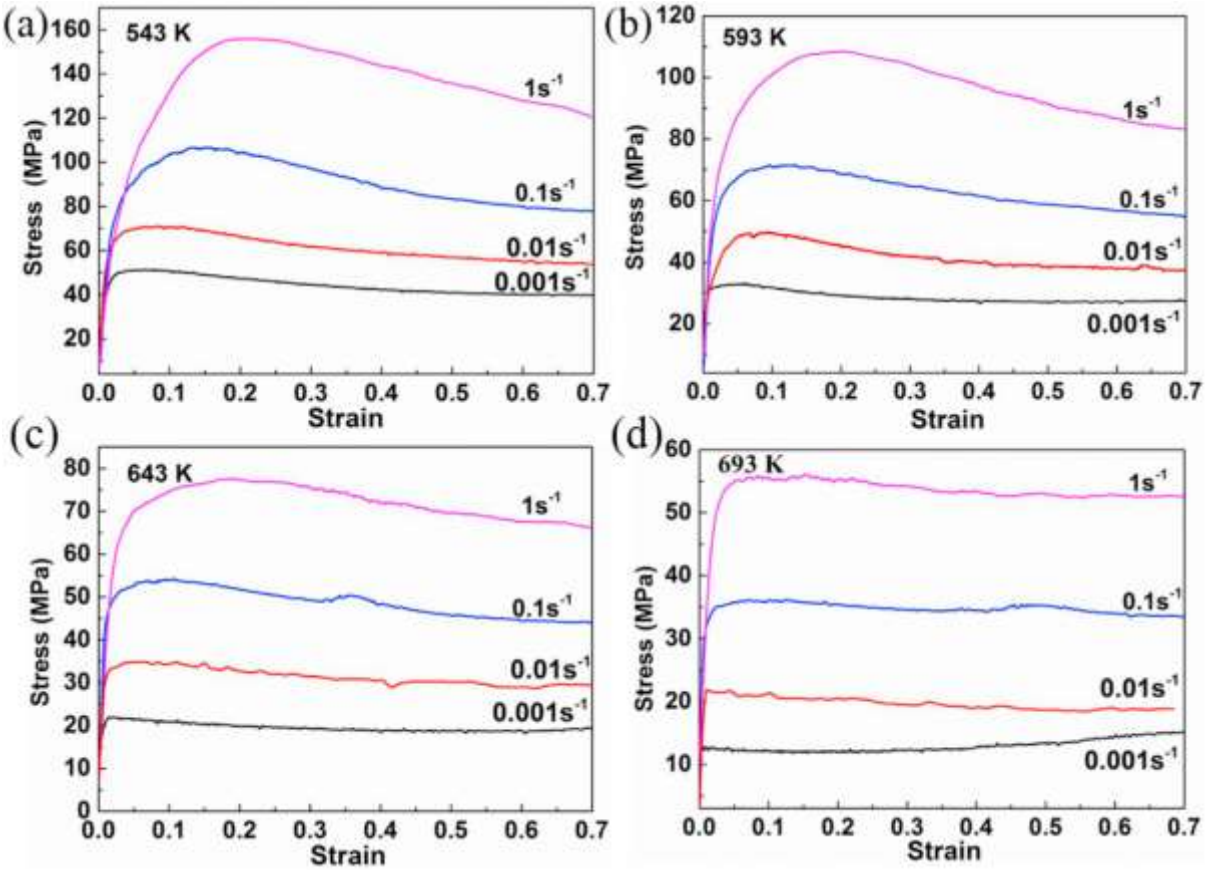

Fig. 1: True stress-strain curves of the 3 vol% 20 mm SiCp/Mg-Zn composite at different temperatures.

This promotes the annihilation of dislocations and reduces dislocation density inside the composite, which decreases the flow stress [22]. Second, the flow stress curves generally consist of three regions: work hardening, softening and balance of hardening and softening. Work hardening is caused by dislocation multiplication and entanglement, and dynamic softening is the result of annihilation and rearrangement of dislocations [23]. The curves increase to a peak then decrease with the increasing strain, which shows typical softening characteristics at 543-593 K and 0.1-1 s^{-1} in Fig. 1 (a) and (b). While the curves show a steady state with the increase of strain at high temperatures (643-693 K) in Fig. 1 (c) and (d). Additionally, the curve compressed at 543 K and 1 s^{-1} (Fig. 1 (a)) exhibits a concave curvature at 0.1 strain, which is considered as the characteristic of the twinning-dominated deformation [24].

3.2. Microstructure evolutions at different temperatures and strain rates

The stress-strain curves of the composite show that the temperatures and strain rates have an influence on flow stress. It means that the microstructure can also be influenced by temperatures and strain rates. Fig. 7 shows the microstructure of the composite with different strain rates at 543 K. A large number of twins are observed around the SiCp in Fig. 7 (a) at the strain rate of 1 s^{-1}. Dislocation slip is the main mechanism of Mg alloys during the hot deformation process and twins occur when it is difficult for the dislocation slip to proceed. The twins are conducive to coordinated deformation at the initial stage of hot deformation. However, cracks and voids may form along with the twins with the increasing strain. As shown in Fig. 7 (b), twins terminate at the SiCp, indicating that the addition of trace SiCp has an inhibitory effect on the twins. Simultaneously, the dislocations are more likely to be jammed at the intersections of the twins and SiCp due to the hindering effect of the twin boundaries and SiCp on the dislocation movement. And the high dislocation density is beneficial for the nucleation of DRX. Therefore, dynamic recrystallized (DRXed) grains are

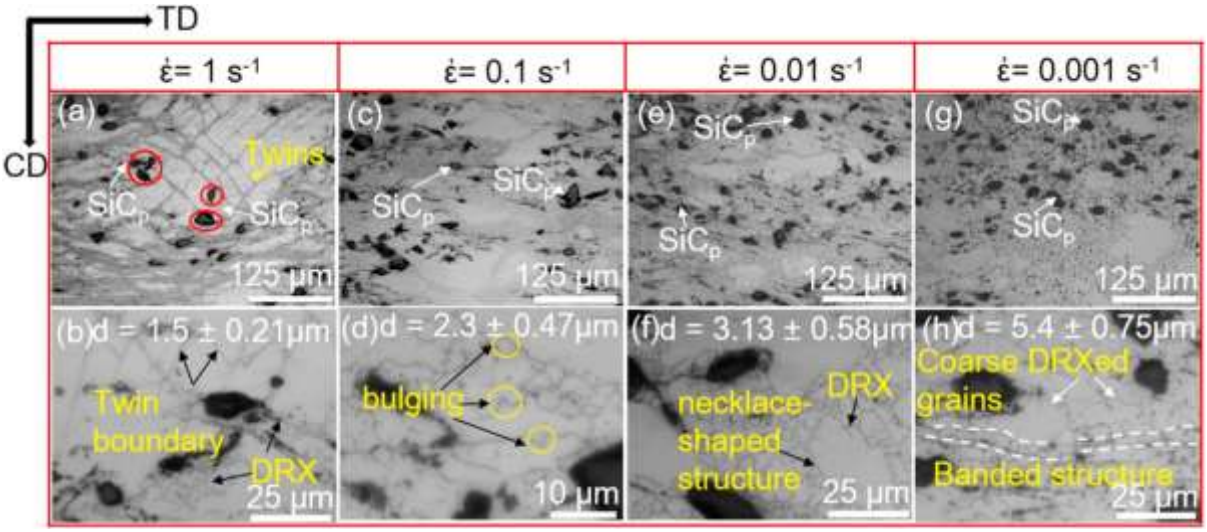

preferentially generated at the intersections of twins and SiCp.

Fig. 7: Microstructure after compression under different strain rates at 543 K. (a) and (b) 1 s^{-1}, (c) and (d) 0.1 s^{-1}, (e) and (f)0.01 s^{-1}, (g) and (h) 0.001 s^{-1}.

Figs. 7 (c) and (d) are microstructures deformed at 0.1s^{-1}. The phenomenon that the grain boundary "bulging" to the adjacent grains can be observed in Fig. 7 (d). Generally, dislocations are continuously absorbed to increase the misorientation between the grain boundary and the matrix during the "bulging" of the grain boundary. Then the nucleation of DRX is developed when the "bulging" radius is greater than the critical nucleus radius. Additionally, the microstructure in Fig. 7 (e) is composed of fine DRXed grains and coarse grains at 0.01 s^{-1}. These fine DRXed grains present a typical necklace shaped structure along the original coarse grain boundaries, as shown in Fig. 7 (f). With the strain rate decrease to 0.001 s^{-1}, a strip structure perpendicular to the compression direction is found in Fig. 7 (h). There are many small grains in the "strip", which are conducive to the grain boundaries sliding during the hot deformation process.

Fig. 8 (a)-(h) are microstructures of the composite with different temperatures at 1 s^{-1}. It can be seen from Fig. 8 (b) that the "strip" structure also exists under the deformation condition of 593 K and 1 s^{-1}. While the "strip" structure disappears as the temperature increases to 643 K, as depicted in Fig. 8 (c). There are small DRXed grains around the SiCp, which is due to the promotion of DRX by PDZ (Fig. 8 (d)). When the temperature increases to 693 K, the bimodal structure is observed in Fig. 8 (f). Fine DRXed grains (~3.6 mm) are generated near SiCp, while coarse DRXed grains (~16 mm) are far away from SiCp. This indicates that the presence of SiCp has a positive effect on the DRX process of the composite. During the hot deformation process, dislocations are accumulated near the SiCp, then DRX occurs when the dislocation density expands to the critical point. Additionally, SiCp hinders the migration of grain boundaries, which results in finer DRX grains near the SiCp.

Moreover, it is believed that the plastic deformation of the magnesium alloy is controlled by dislocation climb at high temperatures (573-723 K) [39,40]. The rapid dislocation climb forms low angle grain boundaries (LAGB), which are transformed to high angle grain boundaries (HAGB) by absorbing dislocations.

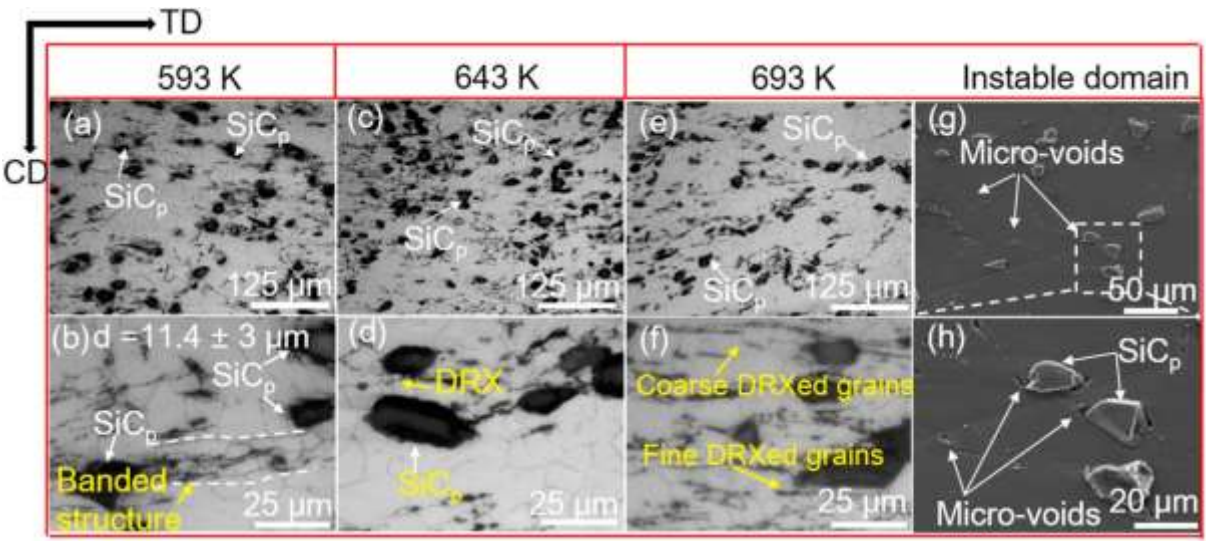

Fig. 8: Microstructure after compression under different temperatures at 1 s^{-1}. (a) and (b) 593 K, (c) and (d) 643 K, (e) and (f) 693 K. (g) and (h) The SEM of the instability regions at 693 K and 1 s^{-1}.

3.3. DRX mechanisms at different regions of the processing map

It has been reported that different regions in the hot processing map correspond to different microstructure evolutions and DRX mechanisms during hot deformation, which needs to be confirmed by microstructure characterization [41]. The microstructure of the instability region (693 K, 1s^{-1}) is shown in Fig. 8 (g) and (h). It can be seen that the micro-voids are mainly concentrated around SiCp. Owing to the mismatch of elastic modulus and coefficient of hot expansion between the matrix and SiCp, the stress concentration is generated during the hot deformation process. And the micro-voids occur at the interface between SiCp-Mg when the stress exceeds the interface bonding strength. Thus, the existence of trace SiCp may reduce the compatibility between matrix and SiCp, which leads to the failure of the composite.

Fig. 9 is the microstructure characterized by EBSD at the region A (543 K, 1 s^{-1}) of Fig. 6 (c) at 0.69 strain. Fig. 9 (b) is an EBSD IPF map. The microstructure is composed of fine DRXed grains and coarse deformed structures. The white areas in Fig. 9 (b) are the unindexed SiCp, which can be proved by Fig. 9 (a). Fig. 9 (c) is the kernel average misorientation (KAM) map, reflecting the dislocation density in the composite [42]. It can be seen from Fig. 9 (c) that the dislocation density around SiCp is higher than that far away SiCp, which provides necessary conditions for PSN. Meanwhile, the high dislocation density in fine DRXed grains (<1 mm) in the vicinity of SiCp reflects the DRX process is in the initial stage and the fine DRXed grains have not grown up due to the short time under high strain rate. Fig. 9 (d) is the pole figure and inverse pole figure. The compression direction and transverse direction are represented by CD and TD, respectively. It can be observed from {0001} pole figure that pole density points are concentrated at both ends of the CD, and the value of texture intensity is 34.4. Additionally, the inverse pole figure shows a higher concentration of the preferred

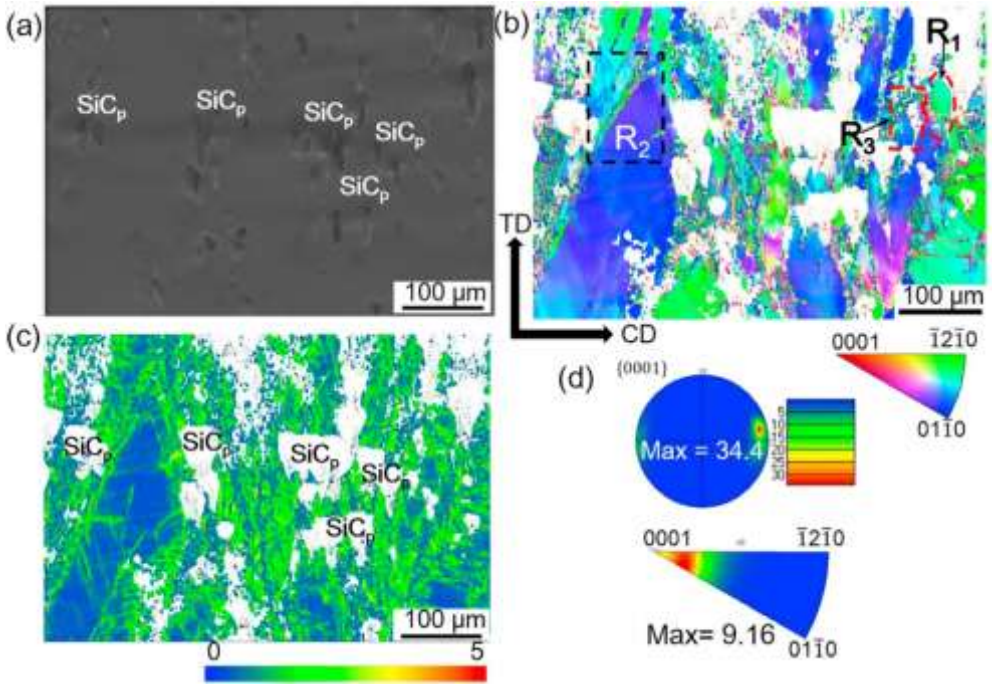

misorientation axis close to

Fig. 9: The EBSD results of the SiCp/Mge5Zn composite at 543 K, 1 s^{-1}. (a)The Backscattered SEM image. (b)The IPF map. (c) The KAM map. (d) The Pole figure and inverse pole figure.

[0001]. Therefore, the compression samples deformed at 543 K and 1 s^{-1} have a strong c-axes//CD texture.

Fig. 10 (a) is the IPF map of the coarse deformed grains (marked as P1-P6) separated from Fig. 9 (b). The basal planes of P1-P6 are all perpendicular to the CD direction. It can be explained that the basal slip system has lower critical stress (CRSS) and operates at the initial stage of hot deformation. Thus the easier mobility of the basal slip systems makes the basal planes rotate to the normal of CD. Consequently, the caxis of these deformed grains is parallel to CD. Furthermore, the grain with c-axes tending to align the direction of CD is hard-oriented grains for basal slip activity, so the coarse grains (P1eP6) are caused by the sluggish DRX in original grains with hard-orientation. Additionally, the projection of these coarse deformed structures in {0001} pole figure gathers at the ends of CD, which shows that P1-P6 grains contribute greatly to the c-axes//CD texture.

Three typical regions (R1-R3) in Fig. 9 (b) are selected to analyze the DRX mechanism of the sample deformed at 543 K and 1 s^{-1}. Fig. 10 (b) is the IPF map of R1. Fine DRXed grains are formed along the coarse matrix grain boundaries, which is a typical necklace structure. LAGBs (2~15°) and HAGBs (>15°) are marked in white and black lines, respectively. There are lots of LAGBs within the coarse grains as indicated by red arrows. In addition, subgrains (marked as 1 and 2) are formed within the parent grain (P7). Simultaneously, fine DRXed grains labelled as G3-G6 are formed at the region where the LAGBs accumulated, revealing that the nucleation of DRXed grains is due to the absorption of dislocations in subgrains. The cumulative misorientation in P7 gradually increases to 15° along with the direction AB,

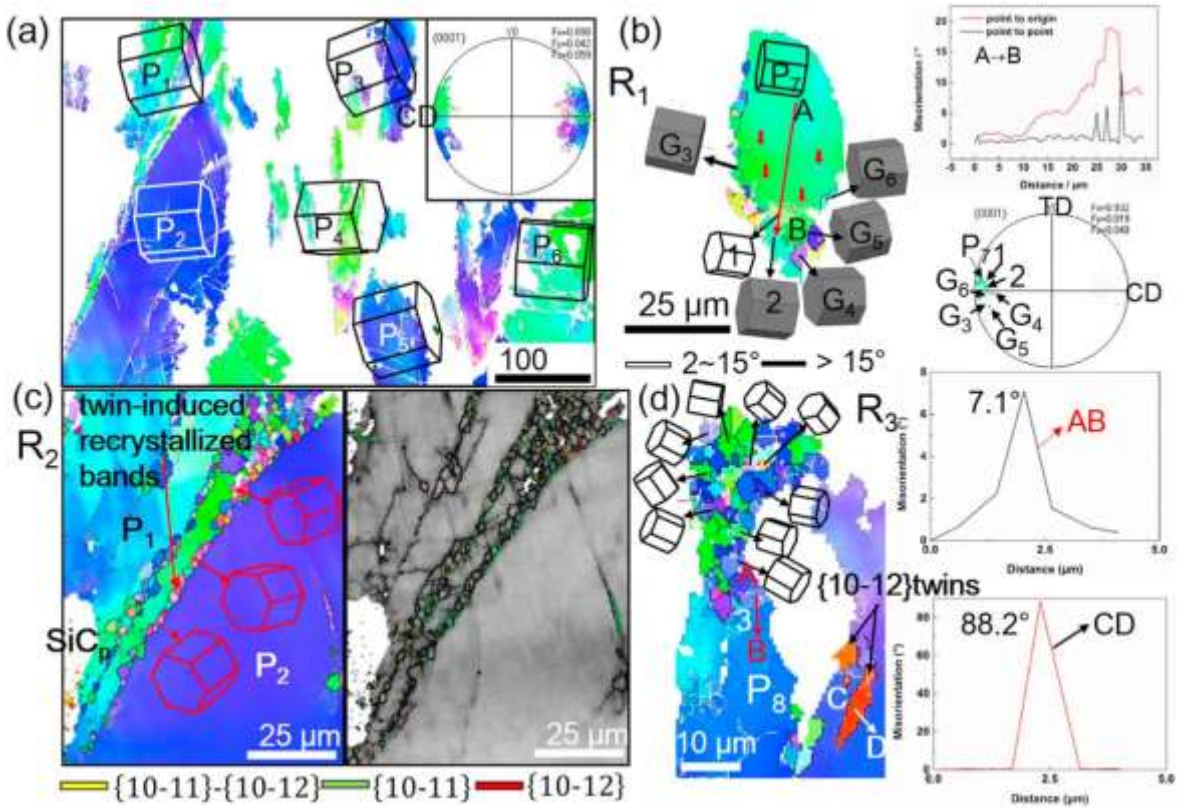

indicating that the

Fig. 10 e EBSD maps of the SiCp/Mge5Zn composite at 543 K and 1 s¡1. (a) EBSD diagram of coarse deformed grains. (b)The IPF map of R1 in Fig. 9 (b). (c) The IPF and grain boundary map of R2 in Fig. 9 (b). (d) The IPF map of R3 in Fig. 9 (b).

dislocation density inside the grain is high, which is beneficial to the formation of subgrains. Generally, LAGBs are formed by the accumulation of dislocations. Then the LAGBs transform into HAGBs by absorbing more dislocations with increasing strain, finally changing subgrains to DRXed grains [43]. The way of the formation of DRXed grains is defined as CDRX mechanism. Besides, the projections of DRXed grains (G3-G7), parent grain (P7) and subgrains (1 and 2) in the {0001} pole figure are shown in Fig. 10 (b). The DRXed grains and sub-grains are both have the same orientation of P7. It is believed that the orientations of new CDRXed grains are close to that of the adjacent parent grains [43].

Fig. 10 (c) is the IPF and grain boundary map of R2. The twin boundaries, including {1012} extension, {1011} contraction and {1011}-{1012} double twin boundaries, are marked in red, green and yellow lines, respectively. The angular deviation to determine the twin boundaries is within 5° of the ideal values. It can be observed that bands of recrystallized grains are distributed around SiCp. The DRXed grain boundaries retain the boundaries of {1011}-{1012} double twins (DTWs) and {1011} compressed twins (CTWs), which can be observed from the grain boundary map. Thus, it can deduce that these DRXed grain nucleation sites may within DTWs and CTWs. There are studies believe that DTWs and CTWs can provide nucleation sites for DRX due to that the basal slip within them is easy to conduct [44]. And the quasi-in-situ EBSD [45] and 3D-EBSD [46] technology are employed to systematically show that DRX preferential nucleation sites are intersections of twins and twins at grain boundaries. In addition, DRXed grains nucleated at DTWs and CTWs stretch along the twin boundaries to form the recrystallized grains band due to the strong blocking effect of twin boundaries on grain growth.

Fig.10 (d) is the IPF map of R3. It can be seen that fine DRXed grains are formed around SiCp, which shows the typical characteristic of PSN mechanism. The PDZ around SiCp contains high-density dislocations, as shown in the KAM map of Fig. 9 (c), causing local lattice rotation in the regions close to SiCp. There are a large number of LAGBs and substructures in the PDZ region, which will be converted to HAGBs through the rotation of the lattice during the deformation process. Therefore, the DRXed grains generated by PSN have a random orientation. There are subgrains (marked as 3) around the SiCp. Line AB in the PDZ is the misorientation between subgrain 3 and parent grain P8, which is 7.1°. This indicates that subgrain 3 is formed by lattice rotation of the local region in parent grain P8. Besides, the misorientation along the direction CD is up to 88.2°, indicating that there are {1012} tension twins (TTWs) around SiCp.

Generally, the nucleation of twins is a process of stress activation. Twins nucleate in the region of local stress concentration such as grain boundaries and second phase particle. Besides, the dislocations accumulate around SiCp at the initial stage of deformation, which also provides conditions for the nucleation of twins [47,48]. Therefore, the twining leads to

the appearance of the instability region at 543 K and 1 s^{-1} in the processing map at 0.1 strain. Depending upon the strain increases, the flow localization introduced by SiCp, leading more dislocations to converge on the boundary of the twins, which promotes DRX within DTWs and CTWs [47]. Meanwhile, DRX within TTWs is difficult to occur owing to the unfavorable orientation of basal slip in TTWs. It is generally considered that TTWs grow, coalesce and intersect with each other during hot deformation. While the addition of SiCp has an inhibitory effect on TTWs, which makes the twins terminate at SiC p (Fig. 10 (d)). The above factors avoid the appearance of cracks, thus making the instability regions disappear with the increase of strains.

Fig. 11 is the microstructure characterized by EBSD at the peak dissipation efficiency region C (693 K, 0.1 s^{-1}) of Fig. 6 (c) at 0.69 strain. As can be seen from the IPF map in Fig. 11 (b), the microstructure is composed of equiaxed DRX grains. Fig. 11 (c) is the KAM map. It can be observed that the dislocation density in the microstructure decreases comparing with Fig. 9 (c) and the dislocations are concentrated in the vicinity of SiCp. With the increase of temperature, the dislocation density in the coarse grains is decreased due to the rearrangement and annihilation of dislocations. Moreover, DRX preferentially occurs in PDZ region around SiCp during hot deformation. The DRXed grains grow up with the increase of temperature, absorbing a large number of dislocations. Meanwhile, the grain boundaries of DRXed grains can also inhibit mobile dislocations, causing the formation of new DRXed grains [49]. So the fine DRXed grains in the initial DRX stage still have high dislocation density. Fig. 11 (d) is the pole figure and inverse pole figure, indicating that the compression sample deformed at 693 K and 0.1 s^{-1} also has a c-axes//CD texture. However, the value of texture intensity is 24.95, which is smaller than the sample deformed at 543 K and 1 s^{-1}. It is due to the increase of DRX that weakens the texture intensity as the temperature increases.

As shown in Fig. 12, three typical regions (R1, R2 and R3) in Fig. 11 (b) are selected to analyze the DRX mechanism. LAGBs (2~15°) and HAGBs (>15°) are marked in white and

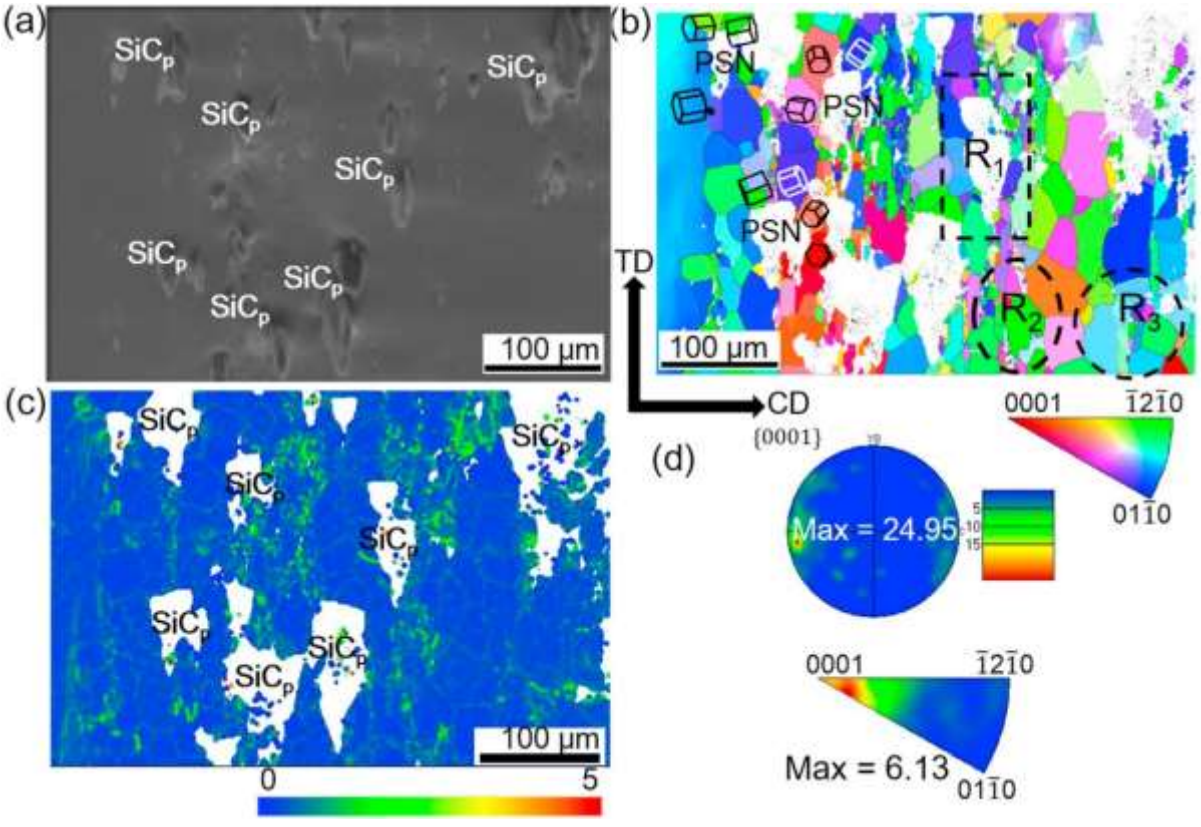

black lines,

Fig. 11: The EBSD results of the SiCp/Mge5Zn composite at 693 K, 0.1 s¡1. (a)The Backscattered SEM image. (b)The IPF map. (c) The KAM map. (d) The Pole figure and inverse pole figure.

respectively. Fig. 12 (a) is the IPF map of R1, it can be observed that SiCp is surrounded by DRXed grains. While when the deformation condition is 543 K and 1 s^{-1}, the DRXed grains only appear in a certain local area around SiCp and there is no obvious DRX inside the coarse matrix grains around SiCp. This is because the increase of temperature improves the deformation coordination between SiCp and the matrix, thus promoting the PSN mechanism. High temperature accelerates the migration rate of subgrain boundaries, thus increasing the misorientation gradient of PDZ. As shown in Fig. 12 (d), the misorientation along the AB and CD directions reached 12.9° and 14.1°, respectively. This proves that the increase of temperature promotes the lattice rotation in the matrix around SiCp. A new DRXed grain will be formed in the PDZ around SiCp if the misorientation of the subgrain exceeds 15°. With the increase of strains, new subgrains are formed by the lattice rotation in PDZ, and then subgrains convert to new grains through absorbing dislocations [50].

The IPF maps of R2 and R3 regions are shown in Fig. 12 (b) and (c). The parent grains (P1eP4) in Fig. 12 (b) show serrated grain boundaries. The grain boundary bulging of P1 is observed to form subgrains with LAGBs. Simultaneously, the fine DRXed grain G1 formed at the serrated grain boundaries and DRXed grains G2 and G3 formed at the triple junctions of parent grains. In addition, it is shown in Fig. 12 (c) that the subgrains (1 and 2) bulge from the parent grain P1. The new small DRXed grain G1 (<5 mm) formed at the triple junctions of the parent grains. Moreover, the DRXed grains (G5 and G6) grow up to approximately 25 mm due to the higher temperatures. The above phenomena provide enough proof of the process of DDRX with the nucleation and nucleus growth at serrated grain boundaries of parent grains by bulging [51]. Also, the orientation relationships of the region R1 and R2 are shown in Fig. 12 (e) and (f). Most of the DRXed grains are randomly distributed without a

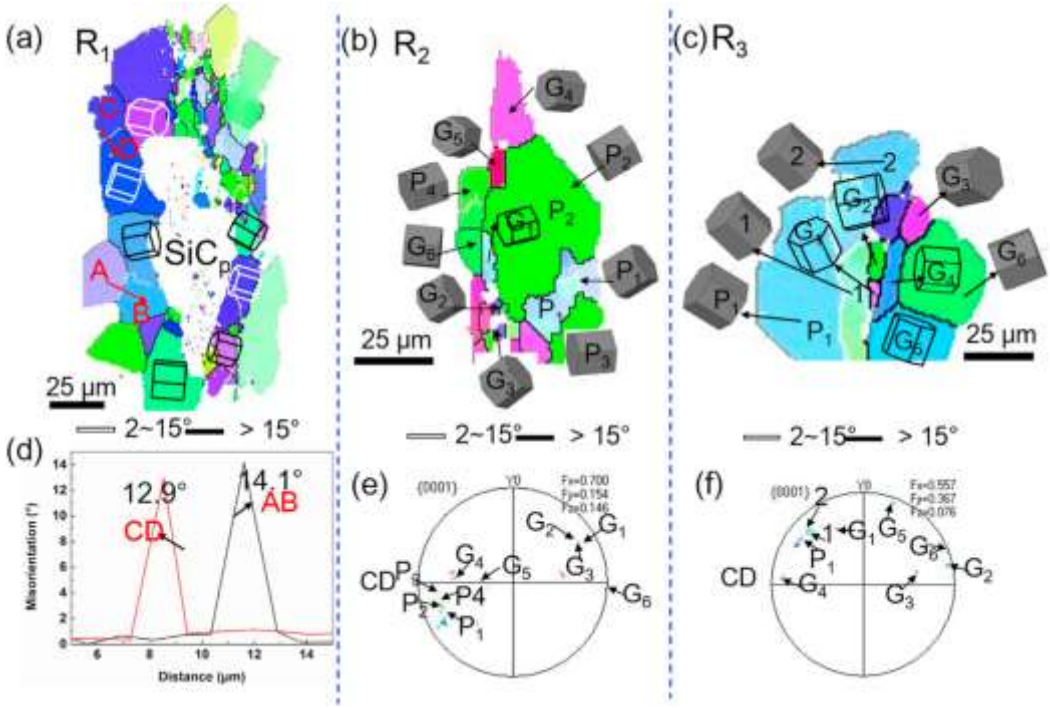

preferred selection of the parent

Fig. 12 e The IPF map of (a) R1, (b) R2 and (c) R3 in Fig. 11. (d) The misorientation profiles along the directions AB and CD. (e) and (f) are the corresponding crystallographic orientation of DRXed grains and sub-grains.

grains, while the subgrains in Fig. 12 (f) have the same orientation as the parent grain, which is the typical feature of DDRXed grains.

The DRXed grains, initial deformed structures and subgrains are distinguished by the Crystallized Fraction Component in Channel 5 software. The different grain types of samples deformed at 543 K, 1 s^{-1} and 693 K, 0.1 s^{-1} are shown in Fig. 13 (a) and (b), respectively, where the deformed grains are indicated in red, the subgrains are marked as yellow and DRXed grains are labelled as blue. Fig. 13 (a) contains a lot of subgrains and deformed structures. While the microstructure in Fig. 13 (b) is mainly composed of the DRXed grains and substructures. And the deformed grains are less in the microstructure. The frequency of different grain types is shown in Fig. 13 (c). It can be seen that the proportion of DRXed grains at 693 K and 0.1 s^{-1} is higher than that of the sample deformed at 543 K and 1 s^{-1}. Therefore, the optimum deformation condition is 693 K and 0.1 s^{-1}.

It is generally considered that hot deformation of polycrystalline metals is carried out by activating slip systems [42]. So the Schmid factor maps for basal ({0001} <a>) slip, prismatic ({1010} <a>) slip and pyramidal ({1011} <a> and {1122} <c-a>) slip are given in Fig. 14 (a)e(h) (Fig. 14 (a)-(d) are at 543 K and 1 s^{-1}, and Fig. 14 (e)-(h) are at 693 K and 0.1 s^{-1}). In addition, the average Schmid factor values are given in the lower-left corner. The regions with red color have a high Schmid factor, meaning that the slip system is easy to activate. As shown in Fig. 14 (a)-(d), basal and pyramidal <a> and <c-a> slip predominate in the sample deformed at 543 K and 1 s^{-1} with the compression continues. While the prismatic slip is difficult due to the low Schmid factor. It can be attributed to the strong crystallographic

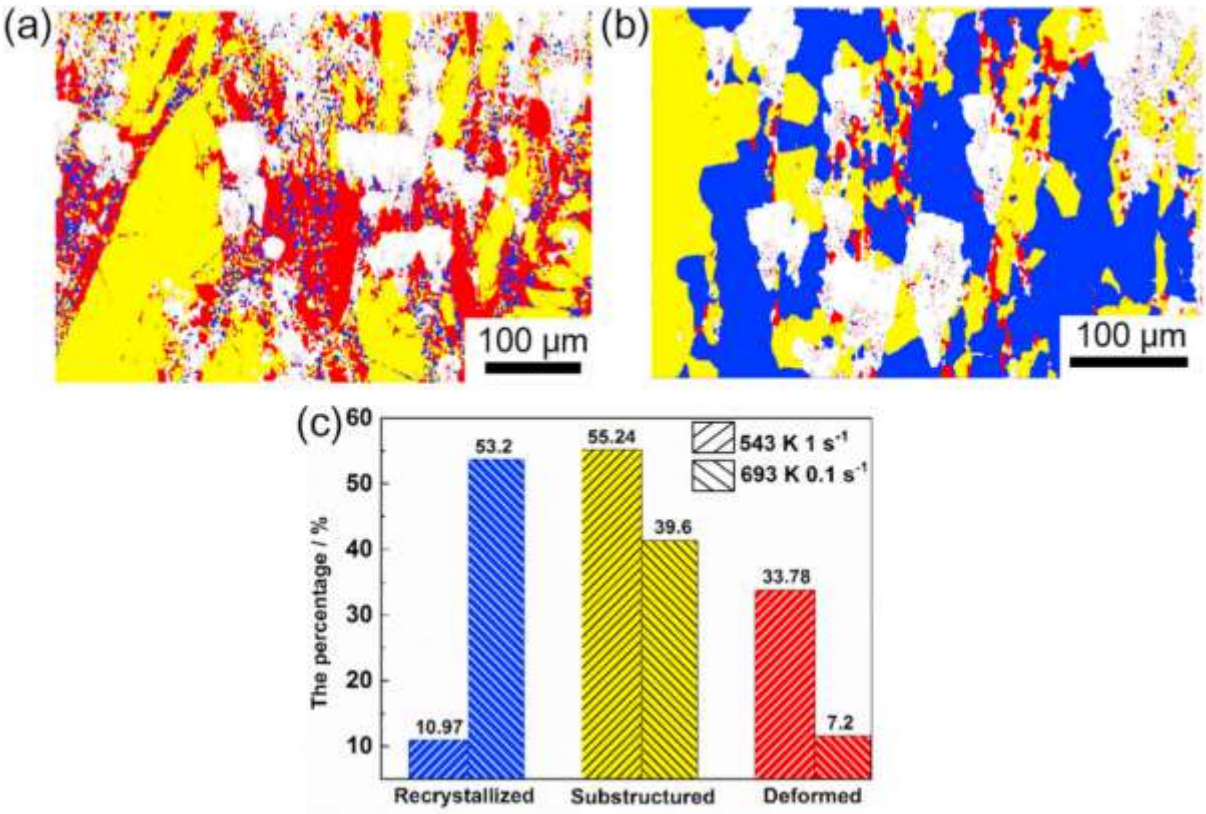

texture with the c-axis

Fig. 13: Different grain types in the microstructure of deformed samples at (a) 543 K, $1s^{-1}$ and (b) 693 K, 0.1 s^{-1}. (c) The grain type frequency of (a) and (b).

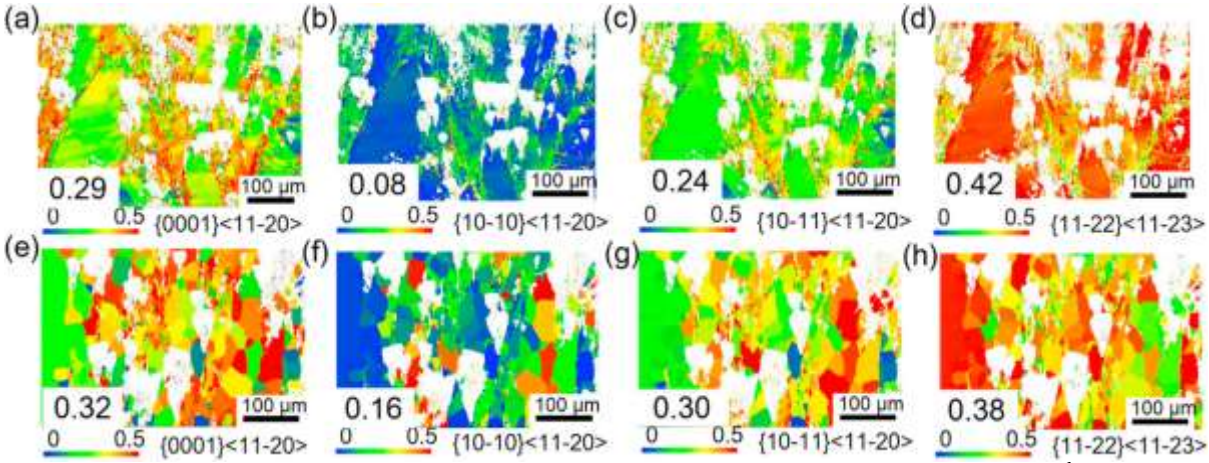

Fig. 14: Schmid factor distribution maps for the deformed sample at (a)-(d) 543 K, 0.1 s^{-1} and (e)-(h) 693 K, 0.1 s^{-1} along CD direction.

aligned with the direction of CD during the hot compression (Fig. 10 (a)), which is not favorable for prismatic slip [52]. While there are more independent systems and higher SFE of pyramidal dislocations, so the cross slip and climb are easier to occur on the pyramidal plane at high temperatures. Thus the formation of HAGBs and DRX is significantly enhanced by the activation of the pyramidal slip. As shown in Fig. 14 (e)e(h), the Schmid factor of prismatic slip increases from 0.08 to 0.16 at 693 K, which is due to the low intensity of c-axes//CD texture. Another reason is the temperature dependence of prismatic slip. Takagi et al. [53] have reported that the shear stress (CRSS) of the prismatic slip in Mg-Zn-Y alloy peaked at ~523 K, while the CRSS value gradually decreases over ~523 K. Generally, the cross-slipped dislocations on the basal plane are difficult to move back onto the prismatic plane due to the high CRSS between the basal and prismatic plane below 523 K. Whereas the CRSS for the cross-slip gliding from the basal plane to the prismatic plane decreases under higher temperature.

4. Conclusion

1. The stress-strain curves of the 3 vol% 20 mm SiCp/Mg-5Zn composite show that as temperature rises or strain rate falls, flow stress decreases. The power strain compensated constitutive function can be used to predict the flow stress.
2. The calculated Q value of the 3 vol% 20 mm SiCp/Mg-5Zn composite is 117.1 kJ/mol, which is less than the reference Mg-5Zn alloy (170.6 kJ/mol). The reason behind the shift in hot deformation behavior from lattice diffusion-controlled dislocation climb to a combination of lattice diffusion and pipe diffusion-controlled dislocation climb is the

high dislocation density in the PDZ surrounding SiCp, which stimulates pipe diffusion. Additionally, as dPDZ increases, the Q value decreases because the PDZ of high dPDZ has a higher dislocation density.

3. The processing map of the 3 vol% 20 mm SiCp/Mg-5Zn composite shows that the instability region is concentrated at 693 K, 1 s^1, and 543 K, 1 s~1. The ideal deformation condition is 693 K and 0.1e0.01s~1. Furthermore, the trace SiC p inhibitory effect on {1012} extension twins and the flow localization-induced promotion of DRX within {1011} contraction twins and {1011}-{1012} double twins are linked to the instability region's disappearance at 543 K and 1 s^1 with strain increase.
4. The DRX mechanisms of 3 vol% 20 mm composite under the deformation condition of 543 K and 1 s^1 are PSN, CDRX, and TDRX, according to EBSD analysis. The primary DRX mechanisms for the composite are PSN and DDRX, operating at 693 K and 0.1 s^1.

References

[1] Zhao Y, Zhang D, Feng J, Chen X, Deng T, Jiang B, et al. Effect of Gd addition on the age hardening response of Mge6Zn-1Mn alloy. J. Mater. Res. Technol. 2020;9(4):8834-41.

[2] Shi QX, Wang CJ, Deng KK, Nie KB, Cao M, Gan WM, et al. Work hardening and softening behavior of pure Mg influenced by Zn addition investigated via in-situ neutron diffraction. Mater Sci Eng, A 2020;772:138827.

[3] Miracle DB. Metal matrix composites e from science to technological significance. Compos Sci Technol 2005;65(15):2526-40.

[4] Zhou Z, Fan Q, Xia Z, Hao A, Yang W, Ji W, et al. Constitutive relationship and hot processing maps of Mg-Gd-Y-Nb-Zr alloy. J Mater Sci Technol 2017;33(7):637-44.

[5] Liu L, Ding H. Study of the plastic flow behaviors of AZ91 magnesium alloy during thermomechanical processes. J Alloys Compd 2009;484(1):949-56.

[6] Wang XJ, Hu XS, Wu K, Deng KK, Gan WM, Wang CY, et al. Hot deformation behavior of SiCp/AZ91 magnesium matrix composite fabricated by stir casting. Mater Sci Eng, A 2008;492(1):481-5.

[7] Prasad YVRK, Gegel HL, Doraivelu SM, Malas JC, Morgan JT, Lark KA, et al. Modeling of dynamic material behavior in hot deformation: forging of Ti-6242. Metall. Trans. A 1984;15(10):1883-92.

[8] Li X, Ren L, Le Q, Jin P, Cheng C, Wang T, et al. The hot deformation behavior, microstructure evolution and texture types of as-cast Mg-Li alloy. J Alloys Compd 2020; 831:154868.

[9] Zhang L, Wang Q, Liu G, Guo W, Jiang H, Ding W. Effect of SiC particles and the particulate size on the hot deformation and processing map of AZ91 magnesium matrix composites. Mater Sci Eng, A 2017;707:315-24.

[10] Srinivasan N, Prasad YVRK, Rama Rao P. Hot deformation behaviour of Mge3Al alloyda study using processing map. Mater Sci Eng, A 2008;476(1):146-56.
[11] Ansari N, Tran B, Poole WJ, Singh SS, Krishnaswamy H, Jain J. High temperature deformation behavior of Mg-5wt.%Y binary alloy: constitutive analysis and processing maps. Mater Sci Eng, A 2020;777:139051.
[12] Zhang X, Zhang Q, Hu H. Tensile behaviour and microstructure of magnesium AM60-based hybrid composite containing Al2O3 fibres and particles. Mater Sci Eng, A 2014;607:269-76.
[13] Lv BJ, Peng J, Wang YJ, An XQ, Zhong LP, Tang AT, et al. Dynamic recrystallization behavior and hot workability of Mge2.0Zne0.3Zre0.9Y alloy by using hot compression test. Mater Des 2014; 53:357- 65.
[14] Zhou SS, Deng KK, Li JC, Nie KB, Xu FJ, Zhou HF, et al. Hot deformation behavior and workability characteristics of bimodal size SiCp/AZ91 magnesium matrix composite with processing map. Mater Des 2014; 64:177-84.
[15] Doherty RD, Hughes DA, Humphreys FJ, Jonas JJ, Jensen DJ, Kassner ME, et al. Current issues in recrystallization: a review. Mater Sci Eng, A 1997;238(2):219-74.
[16] Wu Y, Lavernia EJ. Strengthening behavior of particulate reinforced MMCs. Scripta Metall Mater 1992;27(2):173-8.
[17] Deng K, Shi J, Wang C, Wang X, Wu Y, Nie K, et al. Microstructure and strengthening mechanism of bimodal size particle reinforced magnesium matrix composite. Composites Part A 2012;43(8):1280-4.
[18] Sun XF, Wang CJ, Deng KK, Kang JW, Bai Y, Nie KB, et al. Aging behavior of AZ91 matrix influenced by 5 mm SiCp: investigation on the microstructure and mechanical properties. J Alloys Compd 2017;727:1263-72.
[19] Shi QX, Wang CJ, Deng KK, Nie KB, Wu Y, Gan WM, et al. Microstructure and mechanical behavior of Mg-5Zn matrix influenced by particle deformation zone. J Mater Sci Technol 2021; 60:8-20.
[20] Fan DG, Deng KK, Wang CJ, Nie KB, Shi QX, Wu YC. Improved workability of an Mg-5 wt.%Zn alloy by the addition of trace SiCp. Mater. Today Commun. 2020;25:101474.
[21] Li WJ, Deng KK, Zhang X, Wang CJ, Kang JW, Nie KB, et al. Microstructures, tensile properties and work hardening behavior of SiCp/Mg-Zn-Ca composites. J Alloys Compd 2017;695:2215-23.
[22] Zhong L, Gao W, Feng Z, Lu Z, Zhu C. Hot deformation characterization of as-homogenized Al-Cu-Li X2A66 alloy through processing maps and microstructural evolution. J Mater Sci Technol 2019;35(10):2409-21.
[23] Xu Y, Hu L, Deng T, Ye L. Hot deformation behavior and processing map of as-cast AZ61 magnesium alloy. Mater Sci Eng, A 2013;559:528-33.
[24] Esmaeilpour H, Zarei-Hanzaki A, Eftekhari N, Abedi HR, Ghandehari Ferdowsi MR. Strain induced transformation, dynamic recrystallization and texture evolution during hot compression of an extruded Mg-Gd-Y-Zn-Zr alloy. Mater Sci Eng, A 2020;778:139021.

[25] Hao M, Cheng W, Wang L, Mostaed E, Bian L, Wang H, et al. Texture evolution induced by twinning and dynamic recrystallization in dilute Mg-1Sn-1Zn-1Al alloy during hot compression. J. Magn. Alloys 2020;8(3):899-909.
[26] Yang JY, Kim WJ. The effect of addition of Sn to copper on hot compressive deformation mechanisms, microstructural evolution and processing maps. J. Mater. Res. Technol. 2020;9(1):749-61.
[27] Xu W, Yuan C, Wu H, Yang Z, Yang G, Shan D, et al. Modeling of flow behavior and microstructure evolution for Mg-6Gd-5Y-0.3Zr alloy during hot deformation using a unified internal state variable method. J. Mater. Res. Technol. 2020;9(4):7669-85.
[28] Li Y, Xiao W, Wang F, Hu T, Ma C. The roles of long period stacking ordered structure and Zn solute in the hot deformation behavior of Mg-Gd-Zn alloys. J Alloys Compd 2018; 745:33-43.
[29] Somekawa H, Hirai K, Watanabe H, Takigawa Y, Higashi K. Dislocation creep behavior in MgeAleZn alloys. Mater Sci Eng, A 2005;407(1):53-61.
[30] Koundinya NTBN, Raman L, E NK, Chawake N, Kottada RS. Hot deformation behaviour of Mg-3Al-3Sn and Mg-3Al-3Sn-1-Zn alloys: role of Zn. Materialia 2018;3:274-87.
[31] Liu S, Pan Q, Li M, Wang X, He X, Li X, et al. Microstructure evolution and physical-based diffusion constitutive analysis of Al-Mg-Si alloy during hot deformation. Mater Des 2019;184:108181.
[32] Kim WJ, Chung SW, Chung CS, Kum D. Superplasticity in thin magnesium alloy sheets and deformation mechanism maps for magnesium alloys at elevated temperatures. Acta Mater 2001;49(16):3337- 45.
[33] Zhang L, Su K, Deng KK, Nie KB, Wang CJ, Liang W. Hot tensile behavior and deformation mechanism of Mg-5Ale2Ca alloy influenced by SiC particles. Mech Mater 2020:103599.
[34] Zheng H, Li Z, Chen M, You C, Liu D. The effect of nano b-TCP on hot compression deformation behavior and microstructure evolution of the biomedical Mg-Zn-Zr alloy. Mater Sci Eng, A 2018;715:205-13.
[35] Kwak TY, Kim WJ. Effect of refinement of grains and icosahedral phase on hot compressive deformation and processing maps of Mg-Zn-Y magnesium alloys with different volume fractions of icosahedral phase. J Mater Sci Technol 2019;35(1):181-91.
[36] Chen X, Liao Q, Niu Y, Jia Y, Le Q, Ning S, et al. Comparison study of hot deformation behavior and processing map of AZ80 magnesium alloy casted with and without ultrasonic vibration. J Alloys Compd 2019;803:585-96.
[37] Wang CY, Wang XJ, Chang H, Wu K, Zheng MY. Processing maps for hot working of ZK60 magnesium alloy. Mater Sci Eng, A 2007;464(1):52e8.
[38] Suresh K, Rao KP, Prasad YVRK, Hort N, Dieringa H. Hot forging of Mg-4Al-2Ba-2Ca (ABaX 422) alloy and validation of processing map. Trans Nonferrous Metals Soc China 2018;28(8):1495-503.
[39] Zhang S, Zeng W, Zhou D, Lai Y, Zhao Q. The particle stimulated nucleation in Tie35Ve15Cre0.3Sie0.1C alloy. Mater Lett 2016;166:317-20.

[40] Galiyev A, Kaibyshev R, Gottstein G. Correlation of plastic deformation and dynamic recrystallization in magnesium alloy ZK60. Acta Mater 2001;49(7):1199-207.
[41] Sutton SC, Luo AA. Constitutive behavior and processing maps of a new wrought magnesium alloy ZE20 (Mg-2Zn-0.2Ce). Journal of Magnesium and Alloys 2020;8(1):111-26.
[42] Sun Y, Zhang C, Feng H, Zhang S, Han J, Zhang W, et al. Dynamic recrystallization mechanism and improved mechanical properties of a near a high temperature titanium alloy processed by severe plastic deformation. Mater Char 2020;163:110281.
[43] Jiang MG, Xu C, Yan H, Fan GH, Nakata T, Lao CS, et al. Unveiling the formation of basal texture variations based on twinning and dynamic recrystallization in AZ31 magnesium alloy during extrusion. Acta Mater 2018;157:53-71.
[44] Jiang MG, Yan H, Chen RS. Twinning, recrystallization and texture development during multi-directional impact forging in an AZ61 Mg alloy. J Alloys Compd 2015;650:399-409.
[45] Guan D, Rainforth WM, Ma L, Wynne B, Gao J. Twin recrystallization mechanisms and exceptional contribution to texture evolution during annealing in a magnesium alloy. Acta Mater 2017;126:132-44.
[46] Yi S, Schestakow I, Zaefferer S. Twinning-related microstructural evolution during hot rolling and subsequent annealing of pure magnesium. Mater Sci Eng, A 2009;516(1):58e64.
[47] Lu SH, Wu D, Chen RS, Han EH. The effect of twinning on dynamic recrystallization behavior of Mg-Gd-Y alloy during hot compression. J Alloys Compd 2019;803:277-90.
[48] Xu SW, Matsumoto N, Kamado S, Honma T, Kojima Y. Dynamic microstructural changes in Mge9Ale1Zn alloy during hot compression. Scripta Mater 2009;61(3):249-52.
[49] Pong D, Gottstein G. Necklace formation during dynamic recrystallization: mechanisms and impact on flow behavior. Acta Mater 1998;46(1):69-80.
[50] Chen R, Tan C, Yu X, Hui S, Ye W, Lee Y. Effect of TiB particles on the beta recrystallization behavior of the Ti-2Al-9.2Mo-2Fe-0.1B metastable beta titanium alloy. Mater Char 2019;153:24-33.
[51] Li L, Li H, Jiang W, Pan Z, Wang Y, Wang T. Thermal deformation behavior and processing maps of as homogenized Mg-5.8 Zn-0.5 Zr-1.0 Yb alloy. JOM (J Occup Med) 2019;71(6):2033-9.
[52] Garces G, Perez P, Adeva P. Effect of the extrusion texture on the mechanical behaviour of Mg-SiCp composites. Scripta Mater 2005;52(7):615-9.
[53] Takagi K, Yamasaki M, Mine Y, Takashima K. Temperature dependence of prismatic slip in a single-crystalline long period stacking ordered Mg-Zn-Y alloy. Scripta Mater 2020;178:498-502.